Supporting Information

A spatially confined "double-key lock" smart DNA hydrogel for dynamic detection of microRNA in cells

Liyun Shi,[a,b] Dandan Liang,[b] Jingyu Kuang,[b] Yuting He,[b] Dongyang Wang,[b,*] Jiayi Shan,[b] Ziyang Wang,[b] Wei Shen,[b] Hian Kee Lee[a,b,c,*] and Sheng Tang[a,b,*]

[a]School of Materials Science and Engineering, Jiangsu University of Science and Technology, Zhenjiang 212003, Jiangsu Province, PR China.

[b]School of Environmental and Chemical Engineering, Jiangsu University of Science and Technology, Zhenjiang 212003, Jiangsu Province, PR China

[c]Department of Chemistry, National University of Singapore, 3 Science Drive 3, Singapore 117543, Singapore

*Corresponding authors' e-mail addresses: wangdongyang@just.edu.cn (D. Wang); chmleehk@nus.edu.sg, hiankeelee@u.nus.edu (H.K. Lee); tangsheng.nju@gmail.com, chmts@just.edu.cn (S. Tang).

MATERIALS AND METHODS

Chemicals and materials. The DNA and miRNA oligonucleotides used in this study were synthesized by Shanghai Shenggong Bioengineering Co., Ltd. (Shanghai, China) and purified by high-performance liquid chromatography (HPLC). The relevant sequence information was shown in Table S1. The buffer solution used in the experiment was 1 × TE (40 mM Tris-HCl, 12.5 mM $MgCl_2$, 1 mM EDTA-2Na, pH = 8), and all solutions were prepared with deionized water. Dimethyl sulfoxide (DMSO, 99%), trimethylolaminomethane (Tris), disodium ethylenediaminetetraacetate (EDTA-2Na, 99%) and magnesium chloride ($MgCl_2$, 99.5%) were purchased from Shanghai McLean Biochemical Technology Co., Ltd. (Shanghai, China). Ethanol (EtOH, 99%) were supplied by Jiangsu Qiangsheng Chemical Co., Ltd. (Nanjing, China). Hydrochloric acid (HCl, 12 M) was supplied by Suyi Chemical Reagents Co., Ltd. (Shanghai, China). N-isopropylacrylamide (NIPAM), acrylamide (AM), N,N,N',N'-tetramethylethylenediamine (TEMED) and ammonium persulfate (APS) were supplied by Shanghai Macklin Biochemical Technology Co., Ltd. (Shanghai, China). 1-(3-Dimethylaminopropyl)-3-ethylcarbodiimide (EDC) and N-hydroxysuccinimide (NHS) were purchased from Shanghai Pharmaceutical Group Co., Ltd. (Shanghai, China). T4 RNA ligase 2 and Nb.BbvCI nicking endonuclease were purchased from New England Biolabs (Ipswich, America). Phi29 DNA polymerase was provided by Kangwei Century Biotechnology Co., Ltd. (Taizhou, China).

Apparatus. Deionized water was prepared by Shenzhen Ereeran Water Treatment Equipment Co., Ltd. (Shenzhen, China). Centrifugation was performed using a Sigma 3-15 centrifuge (Osterode am Harz, Saxony, Germany). The pH values of all buffers were determined using the SX-610 digital pH meter (Shanghai Sanxin Instrument, Shanghai, China). Circular dichroism measurements were performed on a J-1500 CD spectrometer (JASCO Corporation, Chiba, Japan). Fluorescence (FL) detection of liquid samples was performed on a NanoDrop 3300 FL spectrophotometer (Thermo Fisher Scientific, Waltham, MA, USA). All the molecular simulations (MD) were performed using the Large-scale Atomic/Molecular Massively Parallel Simulator (LAMMPS-2 Aug 2023). Fourier transform infrared (FT-IR) spectroscopy was conducted using the Alpha IR system (Bruker, Guangzhou, China). The morphology and structure of the prepared samples were characterized by field emission scanning

electron microscopy (SEM) (SU 8020 ESEM, Regulus-8100, Hitachi, Tokyo, Japan) and transmission electron microscopy (TEM) (Talos F200 X, Thermo Fisher Scientific). The solution was mixed using a Vortex-6 oscillator (Kirin Bell Instrument Manufacturing Co., Ltd., Haimen, China). Serum samples were provided by the Affiliated Hospital of Jiangsu University, Zhenjiang, China, and the collection process strictly followed the relevant ethical guidelines and domestic and foreign regulations. The samples were detected by HPLC-fluorescence using an Agilent 1260 Infinity III system.

Development of the HPLC Method. The system integrates core components such as high pressure infusion pump, automatic sampler, column greenhouse and G7121 A fluorescence detector, which can achieve efficient separation and accurate detection. LC solution software was used for data processing. Chromatographic separation The ENorMicro XstrabilisTM C18 column (50 cm × 4.6 mm I.D., 3 μm particle size, Torrance, CA) was used for the separation of various nucleic acids. The column temperature was set at 30 ℃. The mobile phases were K_2HPO_4 (50 mM, pH = 7.0) solution (A) and methanol (B) at 1.0 mL/min. In gradient elution mode, the proportion of methanol increased from 10 to 40% within 20 min.

Preparation of serum samples. Serum samples were centrifuged at 4 ℃ (12,000rpm, 10 min) to remove cellular debris and precipitates, the clear supernatant was obtained as the test original solution, without the need for dilution, extraction, etc. pre-treatment operations. Immediately after, equal-volume aliquots of the clarified serum were prepared to establish a consistent biological matrix background; serial dilutions of exogenous miRNA-21 standards were then added to generate a concentration gradient while maintaining identical matrix composition across all calibration points. The serum matrix test system was prepared by equal division sampling, and different gradient concentrations of exogenous miRNA-21 standards were successively added to ensure that the matrix environment in the system was completely consistent. Subsequently, a series of serum samples containing different concentrations of miRNA-21 were subjected to RCA reactions. After the amplification step, cDNA products of varying concentrations were obtained, thereby achieving signal amplification of the miRNA-21 concentrations. All measurements were carried out in parallel for at least three tests

under strictly controlled reaction parameters to ensure the accuracy of the statistical data. Finally, the linear regression fitting was performed based on the standard addition model, and the background content of miRNA-21 in the serum samples was calculated using the intercept of the correction curve, combined with the slope of the curve, and LOD etc. to evaluate the method's ability to resist matrix interference and quantitative accuracy.

Mechanism of "double-key lock" smart DNA hydrogel for detecting miRNA-21. As depicted in Scheme 1A, the Padlock probe designed to bind miRNA and initiate multiple amplification cycles incorporates two key elements for signal amplification: a hybridization sequence complementary to the miRNA (black) and a nuclease cleavage site (blue). The 5' end of the Padlock probe is phosphorylated, enabling it to specifically ligate and circularize in the presence of the target miRNA template and T4 Rnl2. Subsequently, under the action of Phi29 DNA polymerase, dNTPs are utilized to extend along the circular template, displacing previously synthesized strands, culminating in long single-stranded DNA products with repetitive sequences. Incorporation of Nb.BbvCI specifically recognizes these sites and cleaves the double-stranded sequences, generating a multitude of short cDNA fragments.

Scheme 1B illustrates the responsive behavior of the thermosensitive AIE hydrogel sensor to temperature changes and target amplification products. Initially, a three-dimensional porous network hydrogel is formed through ultrasonication of NIPAM and AM in the presence of the initiator APS and crosslinker TEMED. Thereafter, TCPE fluorophores and acrylamide-modified cDNA-1 and cDNA-2 are covalently bonded to the hydrogel matrix, yielding an AIE hydrogel with a defined lower critical solution temperature (LCST). At ambient conditions, the AIE hydrogel, characterized by a loose porous structure with dispersed TCPE molecules, exhibits weak FL (I). However, upon introduction of RCA products and subsequent incubation at 50 ℃ for 1 h, the AIE hydrogel emits intense FL (II). This is attributed to two primary factors: firstly, when the temperature surpasses the LCST, the porous hydrogel structure collapses from a solvated to a gel state, reducing the macroscopic dimension; secondly, during incubation, the cDNA interacts with the two short complementary sequences (cDNA-1 and cDNA-2) on the hydrogel, reinforcing hydrogen bonding interactions, causing hydrogel contraction and promoting TCPE micro-aggregation and thus emission. When

the temperature returns to room temperature (25 ℃), the hydrogel resumes a homogeneous state below its LCST, yet the established hydrogen bonds between cDNAs remain largely intact, leading to a decrease in FL intensity compared to the peak level observed at 50 ℃ (III). This sequence of events highlights the synergistic interplay of temperature-induced phase transition and specific molecular recognition in the AIE hydrogel, translating target amplification into a discernible optical signal.

Scheme 1C succinctly illustrates the sensor's response when subjected to temperature variations in the absence of output cDNA. As depicted, when the temperature exceeds the LCST, the hydrogel exhibits its characteristic temperature-responsive behavior, leading to a slight enhancement in FL due to the physical changes in the gel structure. Conversely, upon returning to temperatures below the LCST, the hydrogel reverts to a sol state, accompanied by a reduction in FL to a weak level, devoid of any observable AIE characteristics. This integrated approach stands to significantly enhance the sensitivity and specificity of miRNA-21 assays, advancing the frontier of molecular diagnostics and biomarker research.

The mechanism of the influence of solvents on the FL intensity of TCPE.

A pronounced decrease in fluorescence intensity is observed upon increasing f_w from 90% to 99%. This phenomenon can be explained by the following two aspects:

(i) Concentration quenching via aggregation: At f_w = 99%, the aqueous solubility of TCPE is severely limited, leading to pronounced molecular aggregation. This results in locally elevated fluorophore concentrations, which enhance intermolecular interactions, thereby facilitating Forster resonance energy transfer (FRET) and collision-mediated non-radiative decay consistent with classical aggregation-caused quenching (ACQ) behavior. Critically, the reduced interfluorophore distance suppresses radiative recombination, thereby attenuating the overall FL output.[1]

(ii) Formation of non-radiative H-aggregates: The highly aqueous environment promotes the assembly of TCPE into densely packed, face-to-face stacked H-aggregates. At f_w = 99%, this specific supramolecular arrangement accelerates non-radiative relaxation of the excited state and markedly reduces the system's FL quantum yield. Analogous concentration-dependent quenching behavior has been consistently reported across diverse ACQ- and AIE-active systems, underscoring that this response

reflects an intrinsic photophysical property of TCPE rather than an experimental artifact.[2]

Optimization of the reaction conditions for RCA. To further improve the analytical performance of the RCA system, we performed a systematic optimization of key enzymatic and substrate concentrations, including T4 RNA ligase, Phi29 DNA polymerase, dNTPs, and Nb.BbvCI restriction endonuclease as summarized in Figure S5. Firstly, the concentration of T4 DNA ligase was varied from 2 to 7 U (Figure S5A). FL intensity significantly increased with the increase in T4 RNA ligase concentration and stabilized beyond 6 U, indicating that adding excessive T4 RNA ligase could not further amplify FL signal. thus, 6 U was adopted as the optimal concentration. Subsequently, Phi29 DNA polymerase concentration was optimized over the range of 0.5 - 3 U (Figure S5B). FL intensity rose steadily up to 2 U, after which it declined, likely due to non-specific amplification or enzyme-induced background noise. Accordingly, 2 U was determined as the optimal reaction concentration. Further optimization of dNTP concentration (3 mM to 5.5 mM) was carried out. As shown in Figure S5C, FL intensity gradually increased with the increase in dNTP concentration, reaching the maximum at 5 mM. Beyond 5 mM, FL intensity slightly decreased, possibly due to spatial hindrance effects and spatial limitations. Therefore, 5 mM was established as the optimal dNTP concentration. Finally, the parameters of the Nb.BbvCI endonuclease were optimized to enhance the specificity of the enzymatic cleavage (Figure S5D). A peak in FL output indicative of efficient and selective nicking was achieved at 10 U, confirming this as the optimal concentration for subsequent assays.

The RCA reaction duration was a key variable influencing product yield. While extended durations led to longer amplified products, they also incurred higher time costs and potentially compromised the sensor's sensitivity. To optimize this parameter, agarose gel electrophoresis was employed (depicted in Figure S6), with lanes 5-9 showcasing RCA reactions conducted for 0.5, 1, 1.5, 2, and 2.5 h respectively. As observed, the intensity of bands representing RCA products in the sample wells increased over time, reaching saturation by lane 8. A clear band indicates ample amplification, and thus, a 2 h RCA reaction period was determined to offer the best balance between adequate amplification and efficiency, and was thereby selected as the optimal RCA reaction time.

Theoretical simulation analysis and mechanism of smart DNA hydrogel for miRNA detection. To better understand the influence of temperature and cDNA on the aggregation process of hydrogel and TCPE, molecular dynamics simulations (MDs) were carried out (Figure 4A).[3, 4] The model structures in the MDs were obtained using an open source visualization tool.[5] Four samples, with the smart DNA hydrogel samples before and after recognition of cDNA at 298 K (25 ℃) and 323 K (50 ℃), were used for subsequent simulation experiments. To build the hybrid model, the spatial relationship between different molecular chains was controlled. Among them, 12 cDNA-1, 12 cDNA-2, 100 TCPE, 72 cDNA, and 2500 water molecules were selected for the construction of the hybrid model (Figures 4B-4E). In MDs, to describe the atomic interactions between different molecular chains, the PCFF force field was utilized to account for the interactions in different molecular chains, which has been demonstrated to accurately describe bonds, angles, dihedral angles, and electrostatic interactions in organic molecules.[6] The TIP3P water model, which has been shown to work reasonably well in carbohydrate systems, was used.[7] Periodic boundary conditions were applied in all three directions and the steep descent method was used to minimize the energy in each system. The Velocity Verlet algorithm was adopted for integration. Lorentz-Berthelot mixing rules were adopted for van der Waals interactions for different kinds of atoms. The cut-off distances for electrostatic interactions and van der Waals interactions were 1.2 nm. To ensure that the model in every state fully reacted, each was simulated for 10 s. The relaxation videos of the four states of materials (the smart DNA hydrogel (movie S1) without and (movie S2) with cDNA at 25 ℃, and the smart DNA hydrogel (movie S3) without and (movie S4) with cDNA at 50 ℃) correspond to movies S1-S4, respectively. For each DNA hydrogel model within the first 2 s, it was observed that the initial randomly dispersed molecules (Figure 4B-4E) rapidly gathered into dense three-dimensional porous network structure nanoclusters (Figures 4F-4I). In Figures 4F-4I, the volumes of the four models aggregated from the same initial volume are shown as 103.715^3, 87.31^3, 91.85^3 and 97.07^3 respectively. It is evident that, the smart DNA hydrogel exhibited the most significant volume contraction compared to other models under the influence of temperature and cDNA. Meanwhile, the TCPE molecules were affected by spatial regions, resulting in the greatest degree of aggregation (Figure S7). Figure 4J and 4K demonstrates that hydrogen bonds, van der Waals, and electrostatics are the key interaction forces driving conformational

changes in DNA hydrogels in the four model systems. Compared with other hydrogel models, the smart DNA hydrogel with cDNA at 323K shrank the most in the same time. Therefore, TCPE molecules exhibited the highest degree of aggregation and FL intensity under the action of these forces.

For mean square displacement (MSD) and diffusion coefficients calculation (DCC), to collect dynamics trajectories for subsequent data analysis, the different systems were performed at 298 K/323 K and 1 atm for 20 ns under isothermal-isometric NVT ensemble using Velocity-rescale thermostat with a time step of 1.0 fs.[8] The diffusion coefficients of the ionic species D_{Li^+} were calculated by evaluating the ions' mean squared displacement at long timescales:

$$\bar{D}_{\pm} = \lim_{t' \to +\infty} \frac{\{[X_i(t + t') - X_i(t)]^2\}_{\pm}}{6t'} \quad (1)$$

where t' is the lag time, $X_i(t)$ is particle i's position at time t, and $\{[X_i(t + t') - X_i(t)]^2\}_{\pm}$ stands for an ensemble average. Assuming that the Hamiltonian system presently studied is ergodic, ensemble averages using averages over species and time origins were calculated.

In Figure 4L, the slope of the curve reflects the rate of diffusion motion of TCPE molecules. The differences in MSD growth among different models intuitively demonstrated the degree of restriction of the microstructure of the four models on the motion of TCPE molecules. Due to the double effects of temperature and cDNA, the DNA hydrogel had a dense three-dimensional network structure, which caused the MSD of TCPE molecule to be relatively slow. The quantitative characterization of diffusion coefficient directly reflected the diffusion ability of TCPE molecules in different models (Figure 4M), which is consistent with MSD results.

Experimental figures and tables

Table S1. The sequences of nucleic acid chains considered in the work.

Oligonucleotide	Sequence (from 5' to 3')
Padlock probe	Phosphate-TGATAAGCTACCTCAGCTCAACATCAGTCTGATAA GCTACCTCAGCTCAACATCAGTCTGATAAGCTACCTCAGCTCA ACATCAGT
DNA-1	Acrydite-AAAGCTCAACATCAGTC
cDNA-2	TGATAAGCTACCTCAAAA-Acrydite
cDNA	TGAGGTAGCTTATCAGACTGATGTTGAGC
miRNA-21-Atp1	Acrydite -AAATCAACATCAG
miRNA-21-Atp2	TCTGAAGCTAAAA- Acrydite
miRNA-21	UAGCUUCAGACUGAUGUUGA
M1	UAGCUUAUCAGACCGAUGUUGA
M2	UAGCUAAUCAGACCGAUGUUGA
NM	AUAUCCGGGUUCAGCGGACCCG
miRNA-21	UAGCUUCAGACUGAUGUUGA
miRNA-196a	UAGGUAGUUUCAUGUUGUUGGG
miRNA-155	UUAAUGCUAAUCGUGAUAGGGGU

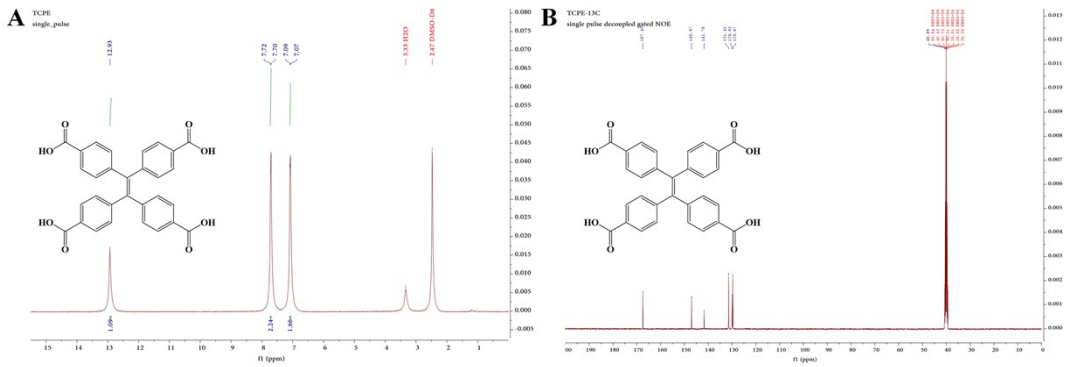

Figure S1. (A) ^{1}H NMR and (B) ^{13}C NMR of TCPE (1,1,2,2-tetra(4-carboxybenzene) ethylene).

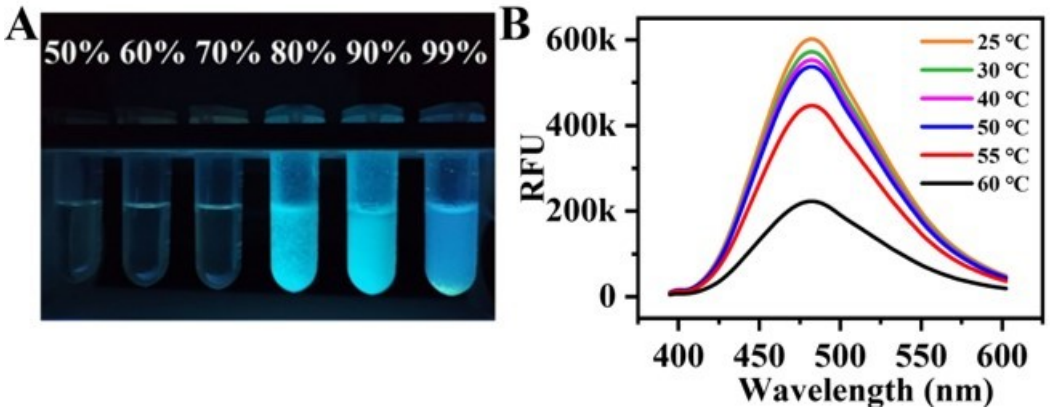

Figure S2. (A) FL photographs of TCPE at different f_w. (B) FL intensity of TCPE at different temperatures.

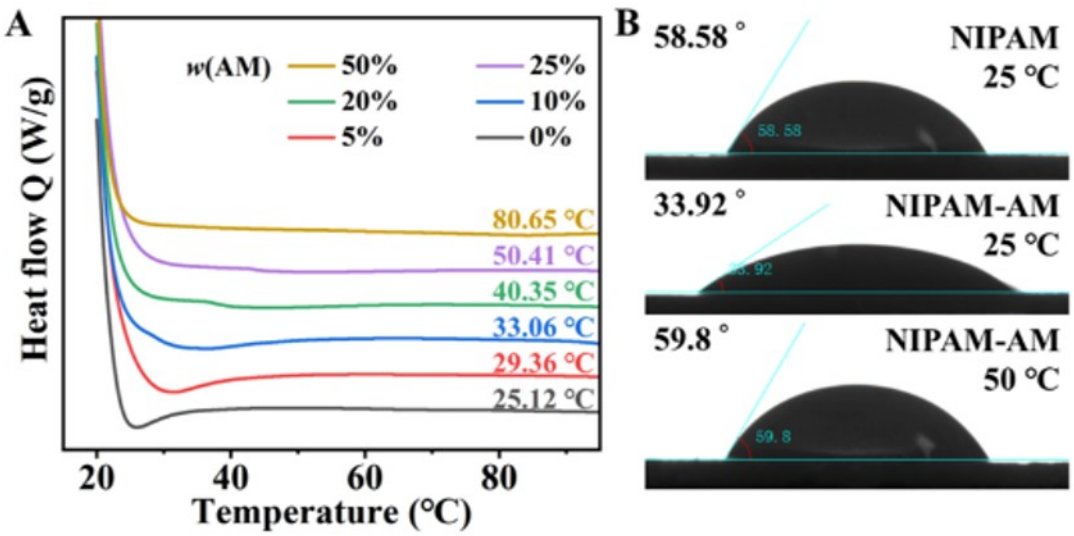

Figure S3. (A) DSC thermograms of the smart DNA hydrogel prepared with different contents of AM. (B) Contact angles of different hydrogels.

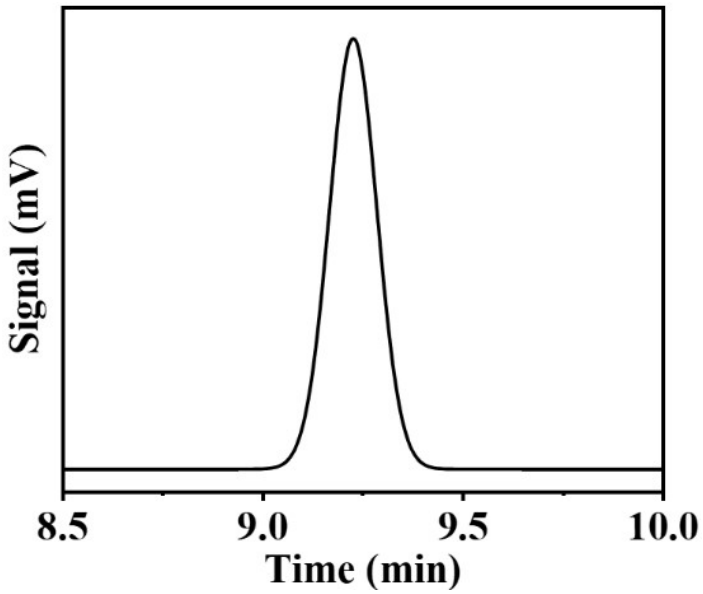

Figure S4. HPLC analysis of cDNA fragments generated from RCA amplification products after Nb.BbvCI cleavage.

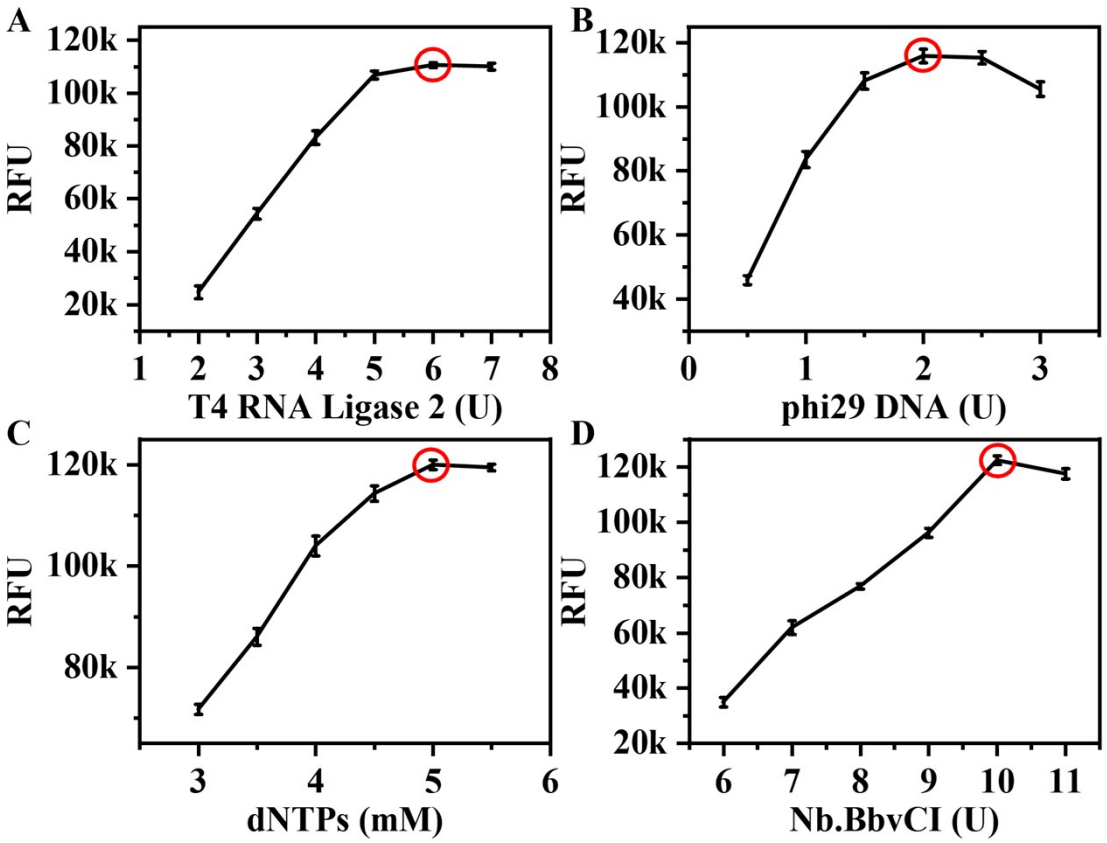

Figure S5. Optimization of experimental conditions related to this method. The concentration of the target miRNA-21 was 1 nM. (A) Concentrations of T4 RNA Ligase 2 from 2 U to 7 U. (B) Concentrations of phi29 DNA from 1.5 U to 3 U. (C) Concentrations of dNTPs from 3 U to 5.5 U. (D) Concentrations of Nb.BbvCI from 6 U to 11 U.

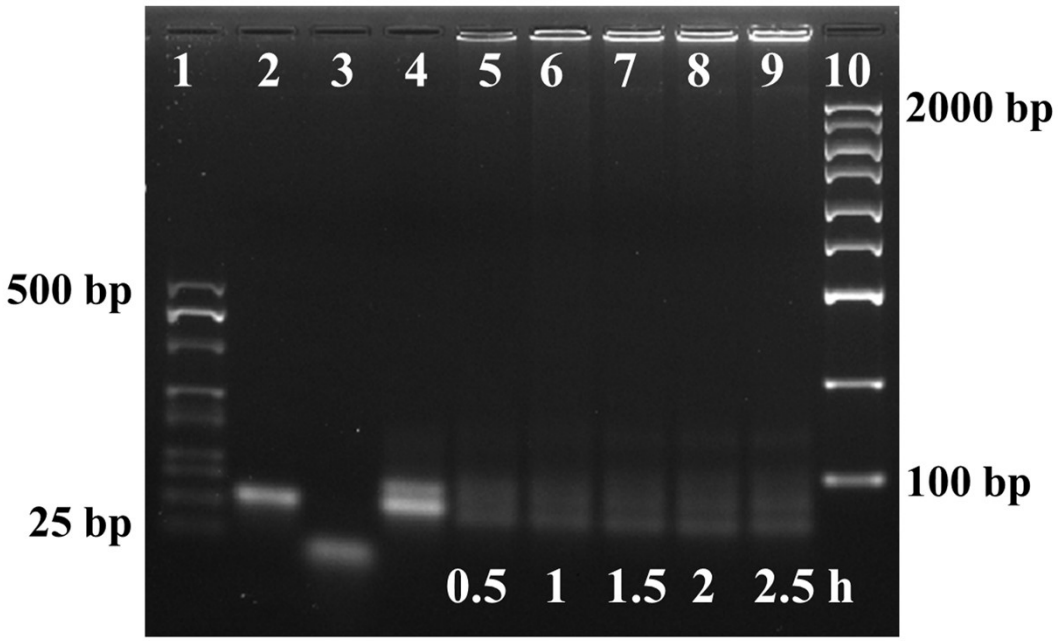

Figure S6. Agarose gel electrophoresis with different RCA reaction times.

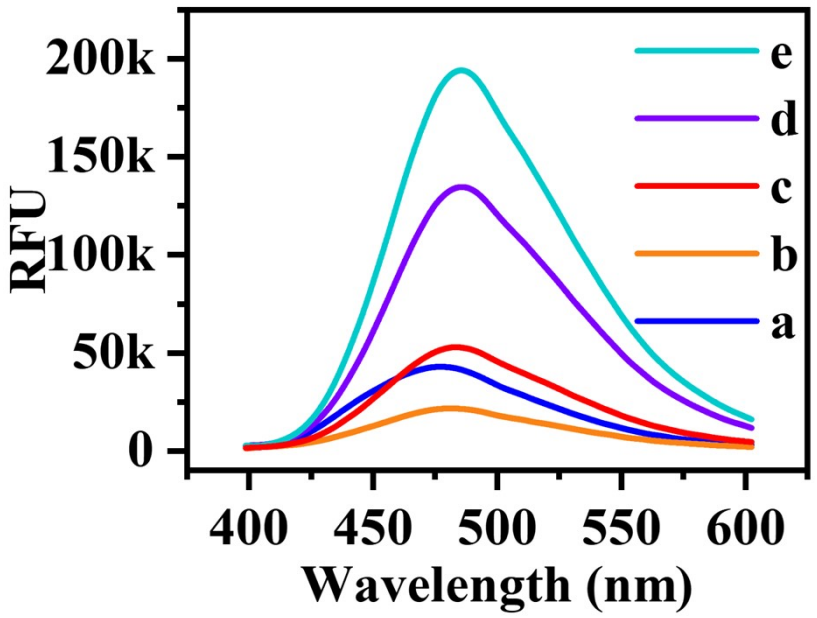

Figure S7. FL spectra of (a-c) the smart DNA hydrogel sensor without cDNA at (b) 25 ℃ and (c) 50 ℃, and (d-e) "dual-key lock" smart DNA hydrogel sensor with cDNA at (d) 25 ℃ and (e) 50 ℃.

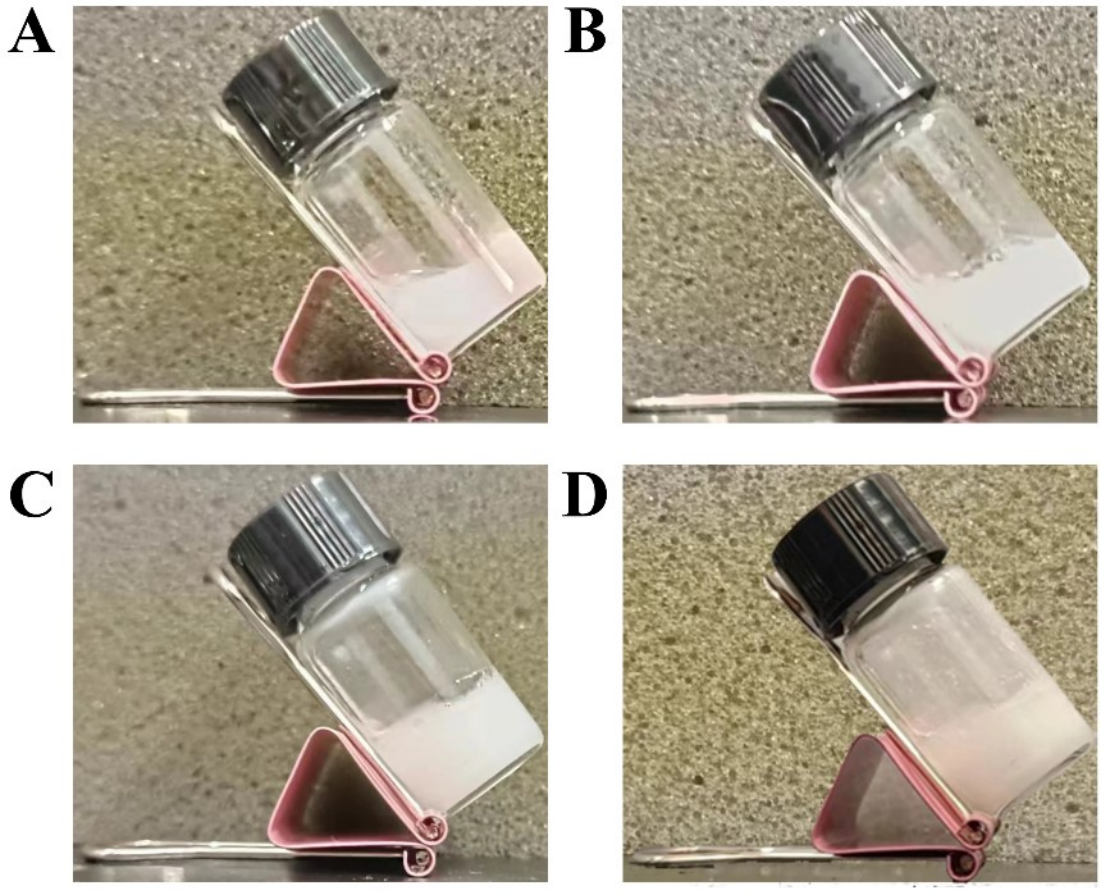

Figure S8. (A-B) Photographs of the smart DNA hydrogel sensor without cDNA at (A) 25 ℃ and (B) 50 ℃, and (C-D) with cDNA at (C) 25 ℃ and (D) 50 ℃.

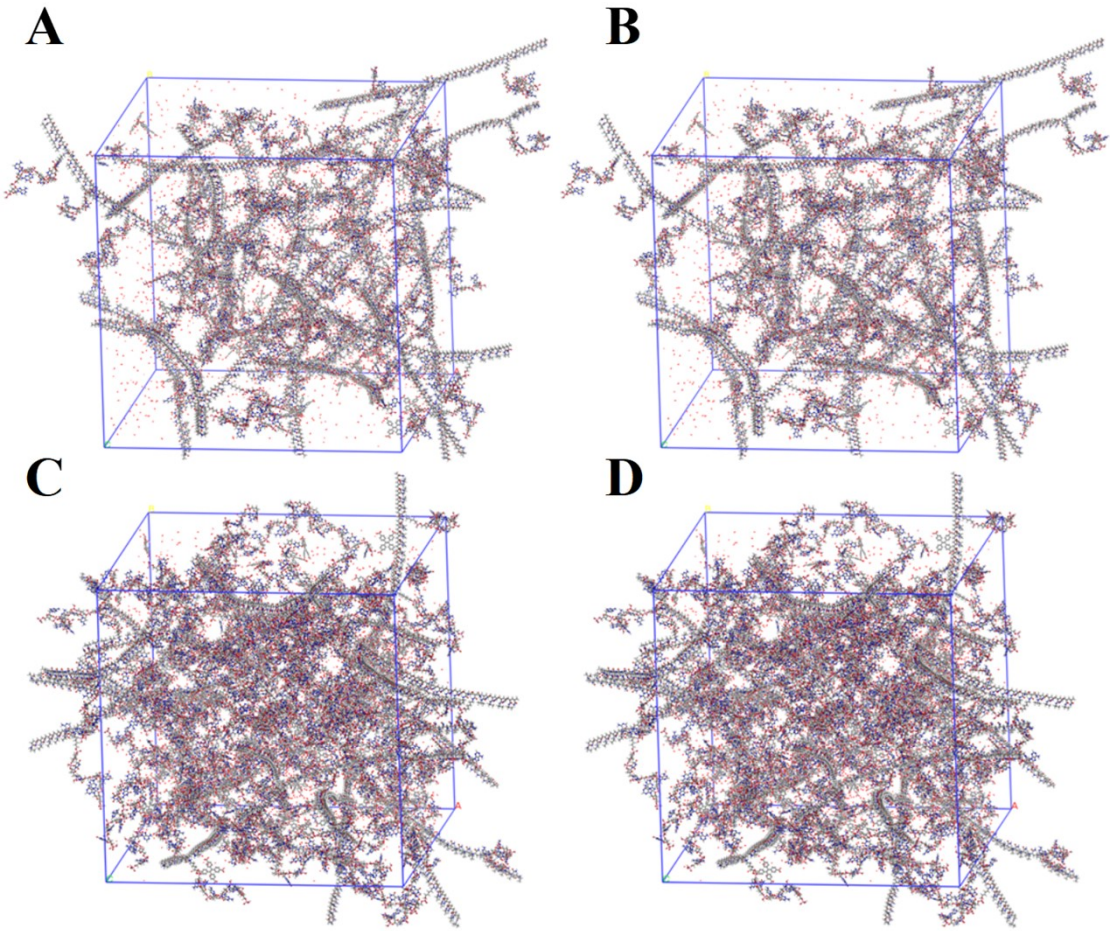

Figure S9. (A-D) Initial MDs of the smart DNA hydrogel (A and B) without cDNA at (A) 25 ℃ and (B) 50 ℃ as well as (C and D) with cDNA at (C) 25 ℃ and (D) 50 ℃.

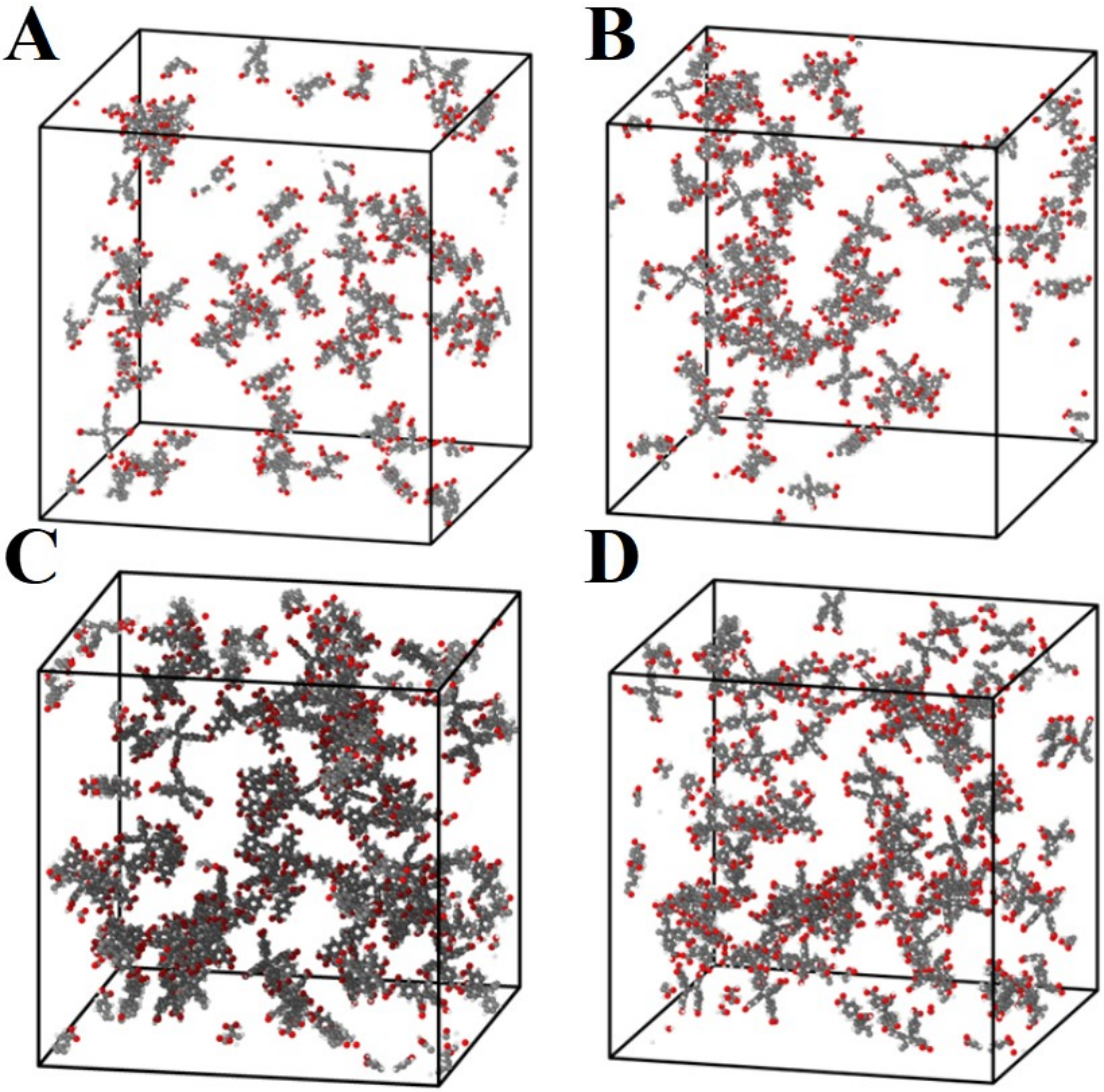

Figure S10. Distribution of TCPE molecules in four state models (A-D) MDs of the smart DNA hydrogel (A and B) without cDNA at (A) 25 ℃ (B) 50 ℃, and (C and D) with cDNA at (C) 25 ℃ (D) 50 ℃.

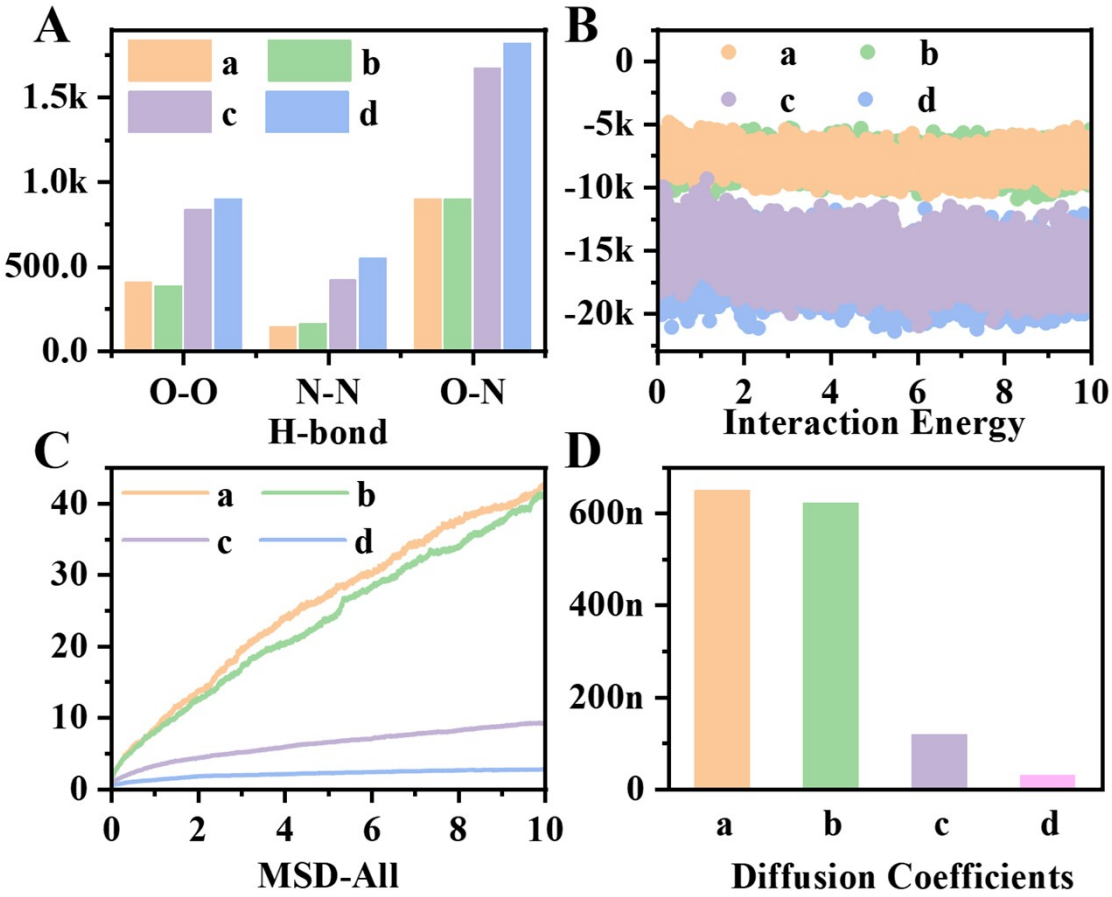

Figure S11. (A) H-bond analysis. (B) Interaction energy analysis. (C) Mean azimuth shift analysis about TCPE. (D) Diffusion coefficient analysis. a-d in Figures S11A-S11D is respectively represented as the MDs models in the states of Figures S9.

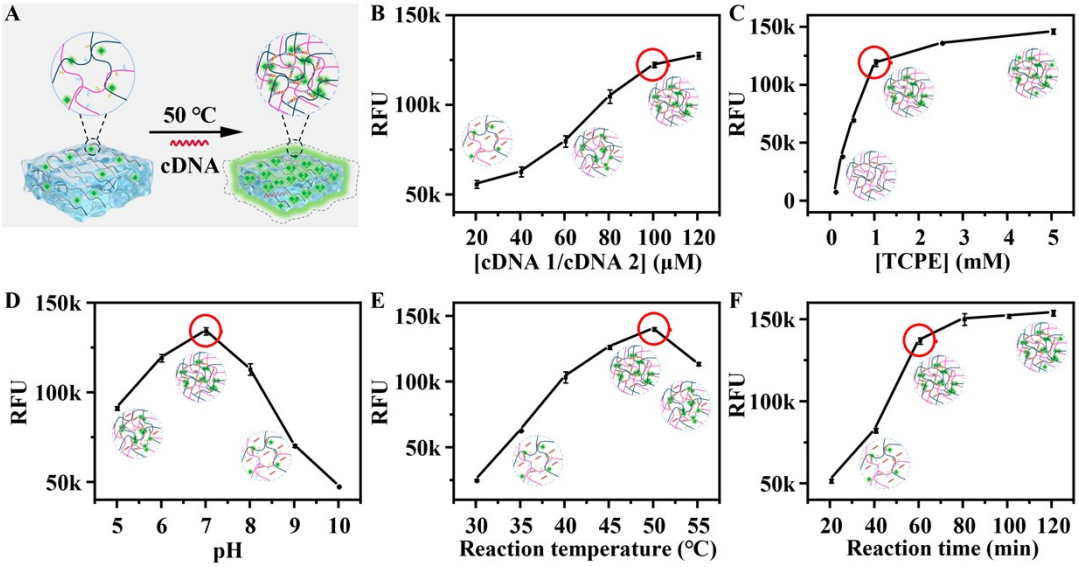

Figure S12. Optimization of experimental conditions related to this method. The concentration of the target miRNA-21 was 1 nM. (A) Schematic of the influence of temperature and cDNA on the analysis performance of the "dual-key lock" smart DNA hydrogel sensor. (B) Concentrations of cDNA-1 and cDNA-2 from 20 μM to 120 μM. (C) Concentration of TCPE from 100 μM to 5 mM. (D) The pH value of the buffer from 5 to 10. (E) Reaction temperature between cDNA strands, from 30 ℃ to 55 ℃. (F) Reaction time between cDNA strands, from 20 min to 120 min. The error bar represents the standard deviation of the three parallel experiments.

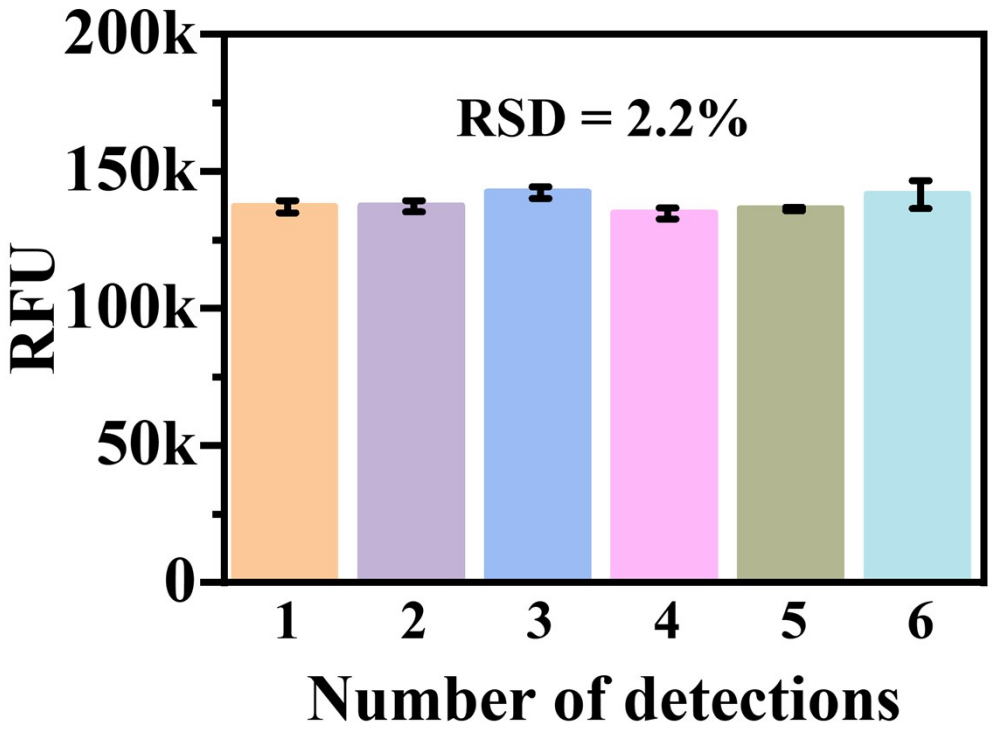

Figure S13. Reproducibility of biosensors constructed by this method in different batches. The error bar represents the standard deviation of the repeated experiment (n = 3).

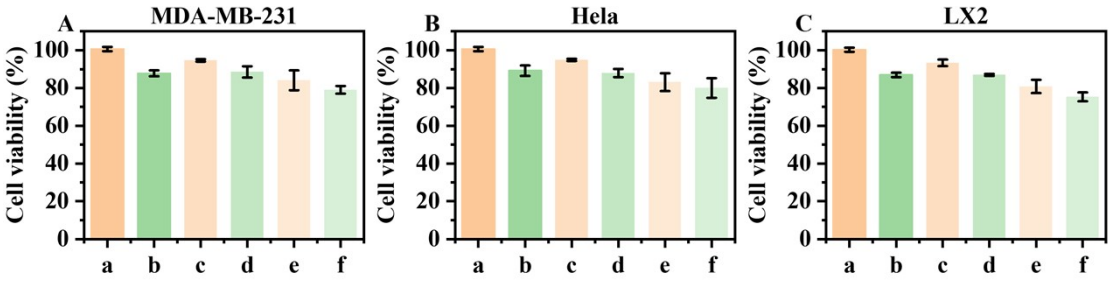

Figure S14. The cytotoxicity of (a) PBS, (b) smart DNA hydrogel at 37 ℃, (c) PBS (d) smart DNA hydrogel at 25 ℃ and (e) PBS (f) smart DNA hydrogel at 50 ℃ after 1 day of culture in (A) MDA-MB-231, (B) HeLa and (C) LX2 cells by the MTT testing kit.

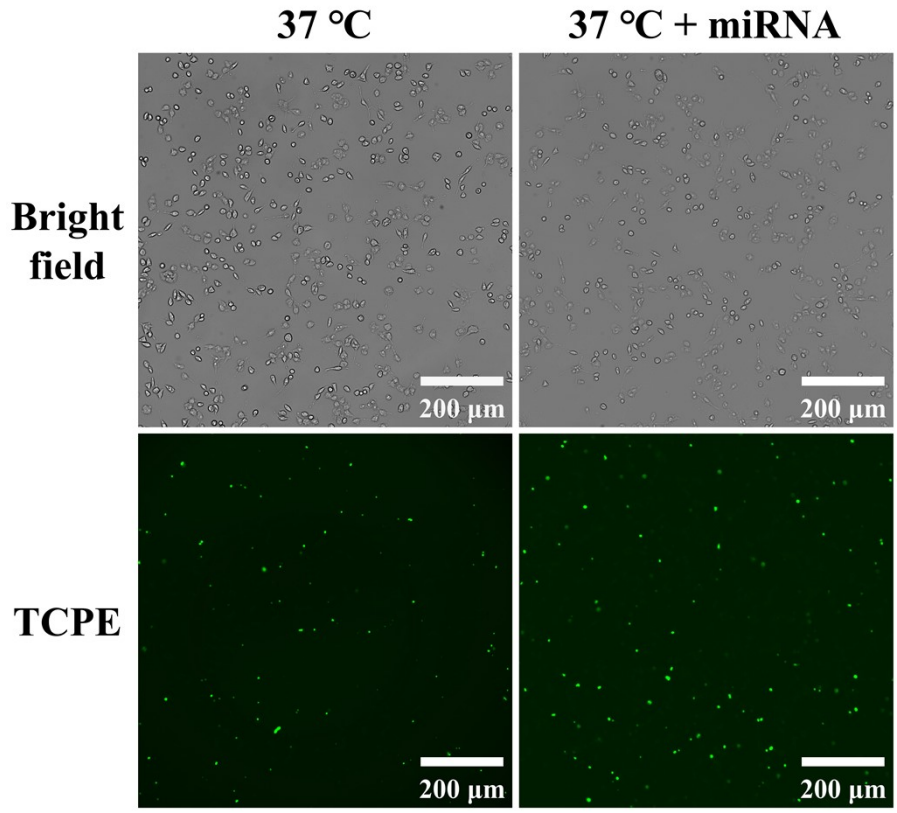

Figure S15. FL micrographs of hydrogel containing MDA-MB-231 cells incubated with 10 nM miRNA-21 at 37 °C for 12 h.

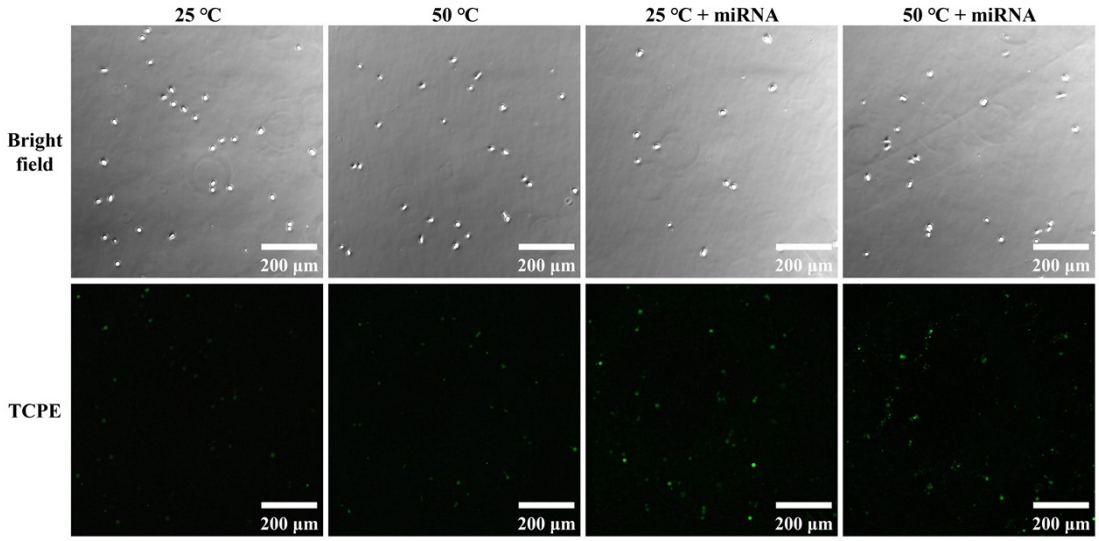

Figure S16. FL micrographs of four hydrogel models containing LX2 cells incubated with 10 nM miRNA-21 for 12 h.

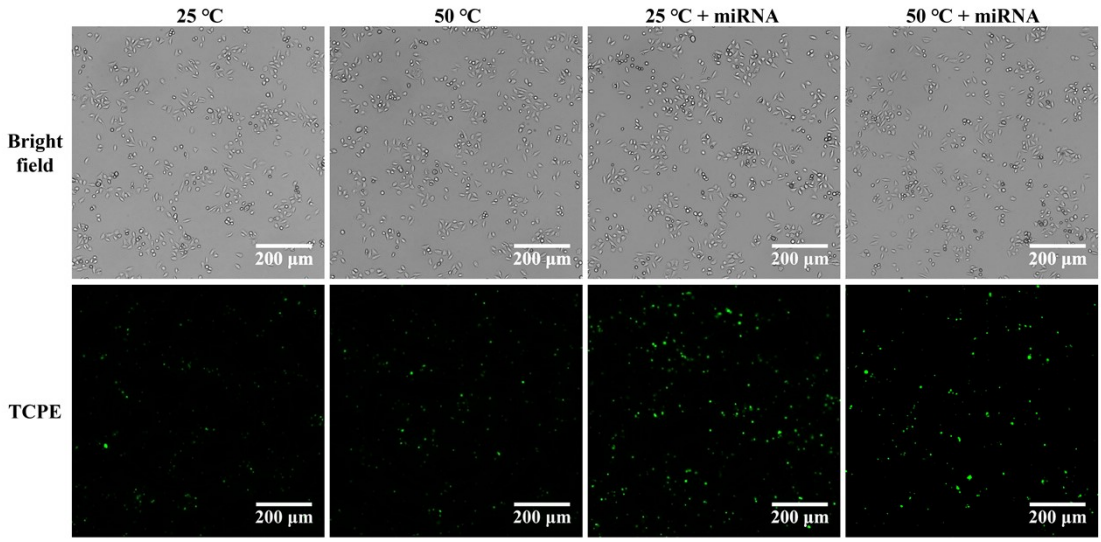

Figure S17. FL micrographs of four hydrogel models containing Hela cells incubated with 10 nM miRNA-21 for 12 h.

Table S2. Comparison of different analytical methods for detecting miRNA.

Analytical method	Target	Sample	LOD	Linear range	Ref.
Electrochemistry	miRNA-21	Human blood serum	4.1 aM	0.1 fM-0.1 nM	[9]
Electrochemiluminescence	miRNA-128	Colorectal cancer	0.17 fM	1 fM-1 nM	[10]
Fluorescence	miRNA-21,	HeLa cells, HepG2 cells, and L02 cells	0.79 pM,	1 pM-10 nM,	[11]
Electrochemical and fluorescent	miRNA-21	Human glioblastoma cells, human monocytic leukemia cells, human embryonic kidney cells, human serum	1.601 fM	5 fM-100 nM	[12]
Surface-enhanced Raman scattering	miRNA-21	Human blood serum	0.62 aM	50 aM-50 fM	[13]
Fluorescence and surface-enhanced raman scattering	miRNA-21	HeLa cells	0.196 fM, 0.165 fM	10 fM-100 pM	[14]
Fluorescence	miRNA-21	MDA-MB-231 cells, Human blood serum	33.3 aM	0.1 fM-10 nM	This work

Table S3. Detection of miRNA-21 isolated from serum samples.

Sample	miRNA-21 (pM)		
	Spiked	This method (RSD%)	RR (%)
Sample 1 Healthy person	Blank	0.047 (2.8)	-
	+0.50	0.551 (3.1)	100.8
	+5.00	5.153 (3.8)	102.1
Sample 2 Healthy person	Blank	0.048 (1.6)	-
	+0.50	0.546 (4.1)	99.6
	+5.00	5.172 (3.5)	102.5
Sample 3 Lung cancer patient	Blank	0.151 (1.8)	-
	+0.50	0.643 (2.6)	98.4
	+5.00	5.142 (3.3)	99.8
Sample 4 Lung cancer patient	Blank	0.178 (2.9)	-
	+0.50	0.696 (4.6)	103.6
	+5.00	5.193 (4.2)	100.3
Sample 5 Gastric cancer patient	Blank	0.226 (3.4)	-
	+0.50	0.732 (2.5)	101.2
	+5.00	5.385 (3.9)	103.2
Sample 6 Gastric cancer patient	Blank	0.263 (2.8)	-
	+0.50	0.750 (3.4)	97.4
	+5.00	5.486 (4.7)	104.5

References for SI only

1 Y. B. Hu, L. Barbier, Z. Li, X. F. Ji, H. Le Blay, D. Hourdet, N. Sanson, J. W. Y. Lam, A. Marcellan and B. Z. Tang, Hydrophilicity-hydrophobicity transformation, thermoresponsive morphomechanics, and crack multifurcation revealed by AIEgens in mechanically strong hydrogels, *Adv. Mater.*, 2021, **33**, 2101500.

2 F. Y. Yang, Y. F. Ou, J. L. Zhou, P. Z. Liang, T. B. Ren, X. B. Zhang and L. Yuan, Hydrogen-bond network-directed controllable assembly of stable cyanine j-aggregates for long-term and high-contrast in vivo imaging, *Angew. Chem. Int. Edit.*, 2026, **65**, e24960.

3 S. Plimpton, Fast parallel algorithms for short-range molecular dynamics, *J. Comput Phy.*, 1995, **117**, 1-19.

4 Y. T. Ji, Y. Yuan, F. M. Peng, S. Y. Fu, B. Liu, Z. Y. Dong, Q. Li, S. C. Ma and Z. M. Ao, Two-component hydrogels built from chinese herbal medicine-derived glycyrrhizic acid and puerarin: assembly mechanism, self-healing properties, and selective antibacterial activity, *ACS Appl. Mater. Interf.*, 2025, **17**, 5223-5231.

5 A. Stukowski, Visualization and analysis of atomistic simulation data with OVITO-the open visualization tool, *Model. Simul. Mater. Sc.*, 2010, **18**, 015012.

6 J. J. Winetrout, K. Kanhaiya, J. Kemppainen, P. J. in 't Veld, G. Sachdeva, R. Pandey, B. Damirchi, A. van Duin, G. M. Odegard and H. Heinz, Implementing reactivity in molecular dynamics simulations with harmonic force fields, *Nat. Commun.*, 2024, **15**, 7945.

7 J. Y. Miao, A. P. Ghosh, M. N. Ho, C. X. Li, X. J. Huang, B. L. Pentelute, J. D. Baleja and Y. S. Lin, Assessing the performance of peptide force fields for modeling the solution structural ensembles of cyclic peptides, *J. Phys. Chem. B*, 2024, **128**, 5281-5292.

8 G. Bussi, D. Donadio and M. Parrinello, Canonical sampling through velocity rescaling, *J. Chem. Phys.*, 2007, **126**, 014101.

9 S. B. Yu, G. L. Wei, P. Zhao, J. Zhang, J. M. Kong and X. J. Zhang, Organic small molecule catalytic PET-RAFT electrochemical signal amplification strategy for miRNA-21 detection, *Chem. Eng. J.*, 2024, **492**, 152380.

10 Y. X. Zhu, Z. H. Liang, P. L. Wang, Q. Ma and Z. Q. Zhang, An electrochemiluminescence sensor with wide stable potential detection window based on superhydrophilic amino acid polyionic liquid for the detection of miRNA-128 in colorectal cancer, *Biosens. Bioelectron.*, 2025, **282**, 117502.

11 Q. H. Jiang, J. Zhou, Y. W. Sha, M. S. Jiang, Y. Q. Chai and R. Yuan, A multifunctional tetrahedral DNA nanostructure for the simultaneous sensitive detection and imaging of miRNA and zinc ions in living cells, *Anal. Chem.*, 2025, **97**, 13368-13375.

12 M. A. Yin, J. Jiao, L. N. Lu, B. X. Hu, L. Xue, F. J. Dai, X. R. Wang, Z. J. Wang, T. Wang and Q. Chen, A simultaneous strategy with multiple-signal amplification and self-calibration for ultrasensitive assay of miRNA-21 based on 3D MNPs-IL-rGO-AuNPs, *Biosens. Bioelectron.*, 2024, **249**, 116009.

13 J. L. Teng, Y. P. Chen, W. W. Zhang, H. T. Xu, L. F. Ke, H. Xu and J. Wang, An RCA-CRISPR-Enhanced SERS platform for ultrasensitive and single-nucleotide-resolved detection of exosomal miRNA-21 in early lung cancer, *Anal. Chem.*, 2025, **97**, 21098-21105.

14 C. H. Liu, J. J. Huang, R. X. Liu, Y. Zhu and T. L. Xu, Target-triggered core-satellite assemblies with fluorescence-SERS cascade amplification for intracellular microRNA detection, *Sens. Actuat. B Chem.*, 2025, **437**, 137759.